



## Full Text View

[Volume 28, Issue 9 \(September 1998\)](#)

### Journal of Physical Oceanography

Article: pp. 1803–1831 | [Abstract](#) | [PDF \(788K\)](#)

# Influence of Stratification upon Diurnal Tidal Currents in Shelf Edge Regions

**Jiuxing Xing and Alan M. Davies**

*Proudman Oceanographic Laboratory, Bidston Observatory, Birkenhead, Merseyside, United Kingdom*

(Manuscript received July 6, 1996, in final form July 11, 1997)

DOI: 10.1175/1520-0485(1998)028<1803:IOSUDT>2.0.CO;2

#### ABSTRACT

A three-dimensional stratified tidal model of the Hebrides shelf area off the west coast of Scotland is used to examine the spatial distribution of the  $M_2$ ,  $O_1$ , and  $K_1$  tides in the region. The model has a finer horizontal finite-difference grid than previous models of the region, with a biharmonic form of horizontal diffusion, and the total variation diminishing scheme for density advection. By this means horizontal diffusion is kept to a minimum and internal tidal effects can be included.

Preliminary calculations assuming a homogeneous sea region show that the model can accurately reproduce the  $M_2$ ,  $O_1$ , and  $K_1$  tidal elevations in the region. An enhancement of the  $O_1$  and  $K_1$  tidal elevations and currents at the shelf edge to the northwest of the Hebrides is found in the model, in agreement with theory and observations. However the enhancement of the diurnal tides, in particular tidal currents along the shelf edge, is larger than that found in the observations, with some regions of local enhancement that are not supported by observations.

Including stratification effects reduces the diurnal tidal currents along the shelf edge and removes the areas of spurious local intensification, giving a distribution in good agreement with observations. A reduction in the amplitude of the diurnal tidal currents at the shelf edge can also be achieved in the three-dimensional model by relating bed stress to depth-mean currents (in essence a two-dimensional model). Although this reduction improves the agreement with observations, regions of spurious intensification still remain, which can only be removed by including stratification effects.

#### Table of Contents:

- [Introduction](#)
- [The three-dimensional](#)
- [Computation of the  \$M\_2\$](#)
- [Frictional influence](#)
- [Concluding remarks](#)
- [REFERENCES](#)
- [TABLES](#)
- [FIGURES](#)

#### Options:

- [Create Reference](#)
- [Email this Article](#)
- [Add to MyArchive](#)
- [Search AMS Glossary](#)

#### Search CrossRef for:

- [Articles Citing This Article](#)

#### Search Google Scholar for:

- [Jiuxing Xing](#)
- [Alan M. Davies](#)

## 1. Introduction

Although two-dimensional tidal modeling is now well established in two separate regimes, namely, shallow sea regions (e.g., [Abraham and Gerritsen 1990](#); [Greenberg 1990](#)) and deep ocean environments (e.g., [Le Provost et al. 1995](#)), using a range of methods from regular finite-difference grids (e.g., [Flather 1988](#)) to boundary-fitted coordinates (e.g., [Spaulding 1984](#)) to the use of finite elements (e.g., [Lynch and Naimie 1993](#)), not a great deal of work has been performed in shelf edge regions, in particular to examine diurnal tides that can be enhanced by a local resonance effect ([Huthnance 1989](#); [Huthnance and Baines 1982](#)).

Some initial two-dimensional modeling of diurnal tides on the Vancouver shelf was performed by [Flather \(1988\)](#) using a regular finite-difference grid and subsequently extended by [Foreman et al. \(1993\)](#) using a finite element approach. Three-dimensional modeling of tides has predominantly been in shallow sea regions and under homogeneous conditions. These models have used a range of approaches in the vertical, namely, an expansion in terms of functions ([Davies 1987](#); [Owen 1980](#)) or a finite-difference grid in sigma coordinates (e.g., the recent work of [Davies and Xing 1995](#)) using a simple flow-related eddy viscosity or a range of turbulence models (e.g., [Davies and Gerritsen 1994](#); [Xing and Davies 1996a](#)) to parameterize the vertical eddy viscosity. Recently both types of models have been used to examine the diurnal tides in the shelf edge region off the west coast of Scotland ([Proctor and Davies 1996](#); [Xing and Davies 1996a](#)). In the majority of these calculations the water was assumed to be homogeneous [[Xing and Davies \(1996a\)](#) did perform a fixed density calculation], although stratification effects are significant in this region ([Ellett et al. 1986](#); [Sherwin 1988, 1991](#)) and can lead to significant  $M_2$  internal tides due to the generation of internal pressure gradients as the tide propagates from the ocean to the shelf ([Baines 1982](#); [Craig 1987](#); [Holloway 1996](#); [New 1988](#); [New and Pingree 1990](#); [Lamb 1994](#)).

In this paper we develop a high-resolution three-dimensional model of the shelf edge region off the west coast of Scotland where the spatial distribution of the  $O_1$  diurnal tide was examined previously ([Proctor and Davies 1996](#); [Xing and Davies 1996a](#)). The grid of the model is significantly finer than those used previously; also the model is stratified and hence the effect of a time-varying (prognostic) density field upon the spatial distribution of the diurnal tides in the shelf edge region off the west coast of Scotland can be considered. Initially calculations are performed assuming the region to be homogeneous, and the spatial distributions of the  $M_2$ ,  $O_1$ , and  $K_1$  (not previously examined in this region) are computed and compared with observations (both elevations and currents). Subsequently calculations are performed with typical winter and summer stratification (see [Fig. 1a](#) , for stratification profiles used in the calculations) to examine its effect upon the  $M_2$  tide, in particular the generation of internal tides, and how it affects the  $O_1$  and  $K_1$  tides in the region. In a final series of calculations the three-dimensional model, assuming a homogeneous sea region, but with bottom friction computed from the depth mean current (in essence a two-dimensional model) is used to examine the influence of bottom friction on diurnal tides. This is a particularly interesting calculation in that a number of simulations (e.g., [Flather 1988](#); [Foreman et al. 1993](#)) have been performed using two-dimensional models in which bottom friction is computed in terms of the depth mean current, and stratification effects have been neglected. Despite the omission of these terms, these models appear to accurately simulate the diurnal tides at the shelf edge. The results from this final series of calculations helps to explain the reasons why these models are successful and the influence of bottom friction on diurnal tides.

The area of the model ([Fig. 1b](#) ) is identical to that used by [Proctor and Davies \(1996\)](#), [Xing and Davies \(1996a\)](#) to study the  $M_2$  and  $O_1$  tide in the region. However, since the model can now generate internal tides, a finer grid ([Xing and Davies 1996a](#)) is required than that used previously (namely, a grid resolution of  $1/12^\circ \times 1/12^\circ$ ). The finite-difference grid of the present model has a resolution of  $1/24^\circ \times 1/24^\circ$  ([Fig. 1c](#) ) and covers a range of water depths from the order of 2000 m to shallow near-coastal regions where depths are less than 10 m ([Fig. 1b](#) ).

The mathematical formulation of the model and the numerical methods used to solve the hydrodynamic equations are discussed in the next section, with subsequent sections dealing with the sensitivity of the diurnal tide to density changes and comparison with measurements.

## 2. The three-dimensional shelf edge model

### a. Governing equations

The three-dimensional equations expressed in transport form using a sigma coordinate in the vertical are given by

$$\begin{aligned} \frac{\partial H\mathbf{v}}{\partial t} + \nabla(H\mathbf{v}\mathbf{V}) + \frac{\partial H\mathbf{v}\omega}{\partial \sigma} - fHu \\ = -gH\frac{\partial \zeta}{\partial y} + \text{BPF}_y + \frac{1}{H^2} \frac{\partial}{\partial \sigma} \left( K_m \frac{\partial H\mathbf{v}}{\partial \sigma} \right) + HF_v \end{aligned} \quad (2)$$

$$\frac{\partial \zeta}{\partial t} + \nabla \left( \int_{-1}^0 (H\mathbf{V}) d\sigma \right) = 0 \quad (3)$$

$$\frac{\partial HT}{\partial t} + \nabla(HT\mathbf{V}) + \frac{\partial HT\omega}{\partial \sigma} = \frac{1}{H^2} \frac{\partial}{\partial \sigma} \left( K_h \frac{\partial HT}{\partial \sigma} \right) + HF_T \quad (4)$$

$$\frac{\partial P}{\partial \sigma} = -\rho gH, \quad (5)$$

where the sigma coordinate is defined by

$$\sigma = (\zeta + z)/H. \quad (6)$$

The inclusion of the total depth  $H$  in these equations is due to expressing them in transport form, which enhances the accuracy of the solution when finite-difference grids are used in regions of rapidly changing topography.

In these equations,  $\mathbf{V} = (u, v)$  and  $(u, v, \omega)$  are the velocity components corresponding to the  $(x, y, \sigma)$  coordinates;  $\rho$  is density;  $T$  is the temperature;  $H$  is the total water depth;  $\zeta$  is the elevation of the sea surface above the undisturbed level;  $z$  is the water depth increasing vertically upward with  $z = \zeta$  the free surface and  $z = -h$  the seabed;  $f$  is the Coriolis parameter,  $g$  is the gravitational acceleration;  $t$  is time;  $K_m$  and  $K_h$  are vertical eddy viscosity and diffusivity coefficients;  $F_u$ ,  $F_v$ , and  $F_T$  are horizontal diffusions for the momentum and temperature;  $P$  is the pressure field. In these equations the baroclinic pressure force terms ( $\text{BPF}_x$ ,  $\text{BPF}_y$ ) are given by

$$\begin{aligned} \text{BPF}_x = \frac{H\partial P_{b0}}{\rho_0 \partial x} \Big|_z - \frac{H}{\rho_0} \left( \frac{\partial(P_b - P_{b0})}{\partial x} + \frac{\sigma}{H} \frac{\partial(P_b - P_{b0})}{\partial \sigma} \frac{\partial H}{\partial x} \right. \\ \left. + \frac{\partial(P_b - P_{b0})}{H\partial \sigma} \frac{\partial \zeta}{\partial x} \right) \end{aligned} \quad (7)$$

$$\begin{aligned} \text{BPF}_y = \frac{H\partial P_{b0}}{\rho_0 \partial y} \Big|_z - \frac{H}{\rho_0} \left( \frac{\partial(P_b - P_{b0})}{\partial y} + \frac{\sigma}{H} \frac{\partial(P_b - P_{b0})}{\partial \sigma} \frac{\partial H}{\partial y} \right. \\ \left. + \frac{\partial(P_b - P_{b0})}{H\partial \sigma} \frac{\partial \zeta}{\partial y} \right), \end{aligned} \quad (8)$$

where  $P_{b0}$  is a reference baroclinic pressure or the initial baroclinic pressure field. The first terms on the right-hand side of [Eqs. \(7\)](#) and [\(8\)](#) are the pressure forces calculated using the  $z$  coordinate. In this way errors due to the coordinate transformation can be reduced. The horizontal diffusion terms  $F_u$ ,  $F_v$ , and  $F_T$  in [Eqs. \(1\)](#), [\(2\)](#), and [\(4\)](#) are parameterized in terms of either a Laplacian or a biharmonic horizontal viscous term. Considering the term  $F_u$  for illustrative purposes, then the Laplacian form is given, in  $z$  coordinate, by

$$F_u = A_m \nabla^2 u = A_m \left( \frac{\partial^2 u}{\partial x^2} + \frac{\partial^2 u}{\partial y^2} \right). \quad (9)$$

The biharmonic form is given by

$$F_u = -B_m \nabla^4 u = -B_m \left( \frac{\partial^4 u}{\partial x^4} + 2 \frac{\partial^4 u}{\partial x^2 \partial y^2} + \frac{\partial^4 u}{\partial y^4} \right), \quad (10)$$

with  $A_m$  and  $B_m$  constant horizontal diffusion coefficients. For temperature and turbulent energy (see later), the diffusion coefficients are denoted by  $A_h$  and  $B_h$ . In the calculations considered later, identical horizontal diffusion coefficients for temperature, turbulence, and momentum were used. The different filtering properties of the Laplacian and biharmonic form of the horizontal diffusion operator are considered in [Heathershaw et al. \(1994\)](#).

A time-splitting method is used to integrate the hydrodynamic equations in order to reduce the computational time, in which the depth-mean currents (external mode) is separated from the depth-dependent velocity (internal mode). Since the external mode represents the fast moving gravity waves, a small time step is required for the time integration of the free surface wave in order to satisfy the CFL condition. The internal mode is, however, integrated with a much larger time step. To avoid the errors in the mass conservation due to the use of the time-splitting method, the sea surface elevation is recomputed before the internal mode equations are integrated by using the depth-mean velocity of the time mean in the smaller time step. The vertical velocity  $\omega$  can be computed diagnostically using the continuity equation.

A staggered Arakawa C uniform finite-difference grid is used in the horizontal with a variable grid in  $\sigma$  coordinates in the vertical. A grid of 50 sigma levels was used in the vertical with a fine resolution of 0.005 in sigma coordinates in the near-bed region. For tidal problems where shear in the surface layer is not significant, a coarser grid resolution could be used ([Davies et al. 1997a,b](#)), whereas it was essential to maintain high resolution in the high shear near-bed region. The vertical diffusion terms, which are computed using a two equation turbulence energy model (see later), are computed by a fully implicit time integration method in order to avoid the use of a short time step when a fine grid is used in the vertical. Details of the method can be found in [Davies et al. \(1997a,b\)](#) and [Xing and Davies \(1996a\)](#). The determination of the vertical eddy viscosity and diffusivity is accomplished using the well-established approach given by [Blumberg and Mellor \(1987\)](#) and [Oey and Chen \(1992\)](#), which involves prognostic equations for the turbulence energy and mixing length that can then be used in the computation of viscosity and diffusivity. A similar approach has been used by [Baumert and Radach \(1992\)](#).

The equations for this turbulence energy model in sigma coordinates are given by

$$\begin{aligned} & \frac{\partial q^2 H}{\partial t} + \nabla \cdot (Hq^2 \mathbf{V}) + \frac{\partial Hq^2 \omega}{\partial \sigma} \\ &= 2 \frac{K_m}{H} \left[ \left( \frac{\partial u}{\partial \sigma} \right)^2 + \left( \frac{\partial v}{\partial \sigma} \right)^2 \right] + \frac{2gK_h}{\rho} \frac{\partial \rho}{\partial \sigma} - \frac{2q^3 H}{B_1 l} \\ &+ \frac{1}{H^2} \frac{\partial}{\partial \sigma} \left( S_q q l \frac{\partial q^2 H}{\partial \sigma} \right) + HF_q, \end{aligned} \quad (11)$$

and

$$\begin{aligned} & \frac{\partial q^2 l H}{\partial t} + \nabla \cdot (Hq^2 l \mathbf{V}) + \frac{\partial Hq^2 l \omega}{\partial \sigma} \\ &= \frac{l E_1 K_m}{H} \left[ \left( \frac{\partial u}{\partial \sigma} \right)^2 + \left( \frac{\partial v}{\partial \sigma} \right)^2 \right] + \frac{l E_1 g K_h}{\rho_0} \frac{\partial \rho}{\partial \sigma} - \frac{q^3}{B_1} W H \\ &+ \frac{1}{H} \frac{\partial}{\partial \sigma} \left( S_q q l \frac{\partial q^2 l}{\partial \sigma} \right) + HF_l. \end{aligned} \quad (12)$$

In these equations  $q^2 = 2E$  with  $E$  the turbulence kinetic energy and  $l$  the mixing length. The wall proximity function  $W$  and the various coefficients  $S_q$ ,  $B_1$ ,  $E_1$  are as defined in [Blumberg and Mellor \(1987\)](#).

The diffusion coefficients for momentum  $K_m$  (namely, eddy viscosity) and density  $K_h$  (namely, eddy diffusivity) are computed from

$$K_m = lqS_M, \quad K_h = lqS_H, \quad (13)$$

with the algebraic form of the stability functions  $S_M$  and  $S_H$  identical to those used by [Galperin et al. \(1988, 1989\)](#) and will not be presented here. A limiting condition ([Galperin et al. 1989](#)) is applied to  $l$ , of the form

$$l \leq \frac{k_1 q}{N^2}, \quad (14)$$

with  $k_1$  a specified constant ([Luyten 1995; Luyten et al. 1996](#)) and  $N^2$  the buoyancy frequency.

### b. Boundary conditions

At the sea surface and sea bed there is no heat flux; thus

$$\left. \frac{\partial T}{\partial \sigma} \right|_0 = 0, \quad \left. \frac{\partial T}{\partial \sigma} \right|_{-1} = 0. \quad (15)$$

This is the usual assumption in internal tide calculations ([Craig 1987, 1988; New 1988; Holloway 1996](#)), in which the temperature field is either taken from the Levitus atlas (as in [Holloway 1996](#)) or, as in our case, from measurement in the area (see later), and the longer-term effects of the surface heat flux are assumed constant over the short period (of order a few days) used in the tidal simulations.

For tidally forced motion the surface stress is zero, thus

$$-\rho \frac{K_m}{H} \frac{\partial u}{\partial \sigma} \Big|_0 = 0, \quad -\rho \frac{K_m}{H} \frac{\partial v}{\partial \sigma} \Big|_0 = 0. \quad (16)$$

At the sea bed a quadratic bottom friction condition is applied of the form

$$\begin{aligned} \left. \frac{K_m}{H} \frac{\partial u}{\partial \sigma} \right|_{-1} &= C_d u_h (u_h^2 + v_h^2)^{1/2}, \\ \left. \frac{K_m}{H} \frac{\partial v}{\partial \sigma} \right|_{-1} &= C_d v_h (u_h^2 + v_h^2)^{1/2} \end{aligned} \quad (17)$$

with  $u_h$  and  $v_h$  components of bed current, and  $C_d$  a coefficient of bottom friction determined from

$$C_d = \left[ \frac{K}{\ln(z_r/z_0)} \right]^2, \quad (18)$$

with  $K = 0.4$  von Kármán's constant,  $z_0$  bed roughness, and  $z_r$  the reference height above the bed at which  $C_d$  and the currents  $u_h$  and  $v_h$  are computed. At the sea surface there is no flux of turbulence energy, and the length scale  $l$  tends to a small value  $z_s$ , which is the sea surface roughness length.

At the sea bed we assume a balance of production, dissipation, and diffusion of turbulence energy, details of which are given in [Xing and Davies \(1996b,c\)](#) and will not be repeated here. This boundary condition is not significantly different from, or produces results very different from, the commonly applied (e.g., [Blumberg and Mellor 1987; Oey and Chen 1992](#)) sea bed boundary condition for turbulence energy namely,  $q^2 = B^{2/3} u_*^2$  with  $u_*$  the bed friction velocity from the

quadratic drag law (see later). At the surface a zero normal flux condition for turbulence energy is appropriate. The length scale at the sea bed is given by the bed roughness length  $z_0$ .

At coastal boundaries the normal component of current, temperature, and turbulence are taken as zero. A radiation-type open boundary condition (e.g., [Martinsen and Engedahl 1987](#)) is applied at sea boundaries, although a number of open boundary conditions was examined. [A recent review of appropriate open boundary conditions can be found in [Davies et al. \(1997a,b\)](#) with details of the application of the flow relaxation zone of [Martinsen and Engedahl \(1987\)](#) as applied to internal tidal problems described in [Holloway \(1996\)](#)]

### c. Hybrid 2D/3D model

In order to compare the effects of various parameterizations of bottom friction upon diurnal elevations and currents in the shelf edge region and make comparisons between three-dimensional and two-dimensional calculations, in some computations the bed stress in the model was derived from the depth mean currents  $\bar{u}$  and  $\bar{v}$  (as in a two-dimensional model) rather than from the bottom currents as in [Eq. \(17\)](#). In this case the bottom boundary condition for velocity becomes

$$\begin{aligned} \left. \frac{K_m}{H} \frac{\partial u}{\partial \sigma} \right|_{-1} &= \bar{k} \bar{u} (\bar{u}^2 + \bar{v}^2)^{1/2}, \\ \left. \frac{K_m}{H} \frac{\partial v}{\partial \sigma} \right|_{-1} &= \bar{k} \bar{v} (\bar{u}^2 + \bar{v}^2)^{1/2} \end{aligned} \quad (19)$$

with  $\bar{k}$  an empirical two-dimensional drag coefficient. When the model is used with this form of bottom friction we shall term it a “hybrid two/three” dimensional (hybrid 2D/3D) model. Under homogeneous conditions and when the vertical integral of the advection and diffusion terms is identical to that used in a two-dimensional model, elevations and depth mean currents computed with the hybrid model are identical to those determined with a conventional two-dimensional model, which have been successful (e.g., [Flather 1988](#); [Foreman et al. 1993](#)) in reproducing diurnal tides along the coast of British Columbia. Hence, comparison of results from the three-dimensional and hybrid model enables us to draw conclusions about the behavior of a two-dimensional model, while still being able to examine the vertical variation of current. However, as we will show later, in order to obtain a good comparison between modeled and computed diurnal tidal currents it is essential to use a full three-dimensional model including stratification effects. The hybrid 2D/3D model should in essence be regarded as a tool to help us understand bottom frictional effects and not as a substitute for a prognostic three-dimensional model.

## 3. Computation of the $M_2$ , $O_1$ and $K_1$ tides

### a. Homogeneous calculation

In order to determine the effects of stratification, an initial calculation (calc 1, [Table 1](#) ) was performed in which the seawater was assumed to be homogeneous. Since the model spans a range of water depths from 2000 m to the order of 10 m in near-coastal areas where bottom friction has an influence, then the  $M_2$  tidal constituent was included in order to obtain the correct frictional level in the model.

In all calculations the tidal distribution was computed by integrating the model forward in time from a state of rest with open-boundary tidal input to the radiation condition. After a “spinup” period of 10 days, computed elevations and currents were harmonically analyzed to determine the tidal constituents in the region.

The drag coefficient  $C_d$  was computed from [Eq. \(18\)](#) with  $z_r$  the reference height, taken as the height of the bottom grid box above the sea bed, and  $z_0$  the roughness length, which was fixed at 0.005 m. Also the biharmonic form of horizontal diffusion, [Eq. \(10\)](#) with  $B_M = 1.0 \times 10^9 \text{ m}^4 \text{ s}^{-1}$ , was used in all calculations rather than the Laplacian form [Eq. \(9\)](#) applied previously by [Proctor and Davies \(1996\)](#) and [Xing and Davies \(1996a\)](#). The biharmonic form rather than the Laplacian was used due to the greater scale selectivity of this form ([Heathershaw et al. 1994](#)).

Consider initially the  $M_2$  component of the tide, computed assuming the water to be homogeneous (calc 1, [Table 2a](#) ). The computed cotidal chart ([Fig. 2](#) ) shows the tidal amplitude increasing significantly from ocean to shelf with tidal amplitudes reaching the order of 1.4 m off the west coast of Scotland ([Fig. 2](#) ). An amphidromic point is situated in the North Channel, with tidal phase increasing northward corresponding to a propagating Kelvin wave. This cotidal chart is not

significantly different from that computed with a coarser grid model ( $1/12^\circ \times 1/12^\circ$ ) by [Proctor and Davies \(1996\)](#) using a model in which the vertical eddy viscosity was related to the flow field, or [Xing and Davies \(1996a\)](#), hereafter referred to as XD96) using an identical grid resolution with viscosity derived from a turbulence energy model.

In order to determine any differences between the  $M_2$  tide computed here and that given in XD96 arising from using a finer horizontal grid and the biharmonic form of the horizontal diffusion term, a detailed comparison of observed and computed amplitude and phase of the  $M_2$  tide at the same coastal and offshore tide gauges used in XD96 and [Proctor and Davies \(1996\)](#) was made ([Table 2a](#) ). In general, the results are comparable with XD96, with root-mean-square (rms) elevation errors slightly lower (8.3 cm cf. 12.6 cm), possibly due to the finer grid although rms phase errors are slightly larger ( $16.5^\circ$  cf.  $12.9^\circ$ ). These differences suggest that, for long-wave processes such as the  $M_2$  tide, the improvement in accuracy, except possibly in near-coastal regions when the grid is reduced by a factor of 2 and the biharmonic diffusion operator is used, is not significant.

Considering now the spatial distribution of  $M_2$  tidal current ellipses at the sea surface and seabed plotted at every fourth model grid point ([Figs. 3a,b](#) ), it is evident from these figures that a near rectilinear tidal flow occurs in the region of the North Channel and the Minch ([Fig. 1d](#) ) with the orientation of the major axis of the ellipse aligned with the orientation of the channel in these regions. An area of reduced tidal current magnitude with near circular current ellipses occurs in the shelf edge region to the west and southwest of the Shetland Islands. Comparing surface and bed current ellipses, it is clear that frictional effects reduce the near-bed currents, although the spatial distribution of ellipses are comparable. Also there are no significant differences in the distribution of ellipses shown here and determined by XD96.

Observed and computed major axis of the current ellipse, its orientation, and sense of rotation at the same 45 locations considered by [Proctor and Davies \(1996\)](#) (see this paper for the exact positions of the data) and XD96 is given in [Table 3](#) . The location of the current meters from which the tidal ellipse parameters have been derived is given in [Fig. 1d](#) , and results in the table progress from the northernmost point (location U, [Fig. 1d](#) ) to the southernmost (location B, [Fig. 1d](#) ). The same letter used in XD96 has been assigned to each location, for ease of comparison.

The set of current meter data collected from the 45 locations was not synoptic, nor can be readily assigned to the typical winter or summer stratified conditions presented in [Fig. 1a](#) . However, as our primary aim here is to see what effect stratification has upon the diurnal tidal currents, this is not an important limitation. As we will show, the inclusion of appropriate stratification has a far greater effect than differences produced by seasonal effects, which can be comparable with errors in the observations, both due to recording and due to harmonic analysis of short period records ([Pugh and Vassie 1976](#)).

The bias in the model at locations R, S, O, L, M, and W to overpredict the current magnitude is consistent with that found by [Proctor and Davies \(1996\)](#) and in XD96. A bias to underestimate current magnitudes was found at locations I, J, and K ([Table 3](#) ), which is also consistent with the results of [Proctor and Davies \(1996\)](#) and XD96. These biases probably reflect errors in the open-boundary input and the uncertainty in the knowledge of water depths in the shelf edge region.

The  $O_1$  and  $K_1$  cotidal charts ([Figs. 4a,b](#) ) show a region of maximum tidal amplitude (amplitudes exceeding 10 cm) in the shelf edge region to the northwest of the Hebrides, with local maxima occurring along the shelf edge to the south of this. The distribution of  $O_1$  co-amplitude and co-phase lines shown in [Fig. 4a](#)  is not significantly different from that found in the coarser grid models of [Proctor and Davies \(1996\)](#) and XD96. The spatial distribution of the  $K_1$  co-amplitude and co-phase lines shown in [Fig. 4b](#)  is similar to the  $O_1$  tide, although amplitudes are larger with a significant difference in phase.

From a comparison of observed and computed  $O_1$  elevation amplitudes and phases ([Table 2b](#) ) at the locations shown in [Fig. 1b](#) , it is clear that the model has a bias to underestimate elevations by the order of 2 cm. A similar bias was found in the models of [Proctor and Davies \(1996\)](#) and in XD96, and is related to the open-boundary input. Phase errors are quite large (exceeding  $30^\circ$ ) at some coastal locations, reflecting the inability of the model, despite the finer grid compared with earlier models, to resolve these near-coastal regions. However, as the main point of the calculations is to investigate the change in the tidal regime in the shelf edge region, which is well resolved in the model, the lack of near-coastal resolution is not a major concern. The enhanced resolution of the present model does, in fact, make a minor improvement in the rms errors, namely (1.88 cm and  $17.20^\circ$ ) compared with earlier calculations (2.13 cm and  $22.31^\circ$ ).

A comparison between computed and observed  $K_1$  tidal elevations and phases is given in [Table 2c](#) . From this table it is evident that the model does not have a distinct bias to overpredict or underpredict the  $K_1$  tidal elevation or phase, with rms errors of 1.91 cm and  $13.5^\circ$  comparable (with phase slightly better) to that obtained previously for the  $O_1$  tide.

Plots of the major and minor axes of the  $O_1$  current ellipse at the sea surface and seabed ([Fig. 5a,b](#) ) show a region of strong (exceeding  $20 \text{ cm s}^{-1}$ )  $O_1$  currents in the shelf edge region to the northwest of the Hebrides, in the area where the surface tidal elevation gradients change most rapidly, with the strongest currents on the shelf. This intensification of the  $O_1$  tide along the shelf edge is due to the fact that the  $O_1$  period (25.82 h) is close to the resonance period of the first-mode shelf wave in this area. The period of this shelf wave in homogeneous conditions is determined by the cross-shelf slope ([Huthnance 1986](#); [Huthnance and Baines 1982](#)), which in the region to the west of the Hebrides is such as to produce a shelf wave with a period close to the  $O_1$  tide, and resonance occurs. A more detailed discussion is given in [Proctor and Davies \(1996\)](#) and will not be repeated here.

It is interesting to note, and this will be discussed further in connection with the influence of stratification, that besides the intensification of the  $O_1$  tide at the shelf edge to the northwest of the Hebrides (at approximately  $58.5^\circ\text{N}$ ) there is another local intensification to the south of this on the shelf edge at about  $57.8^\circ\text{N}$ , with a further intensification at about  $56.6^\circ\text{N}$  corresponding to the local elevation maxima shown in [Fig. 4](#) . Away from these regions over the majority of the shelf and over the oceanic region,  $O_1$  tidal currents are weak (i.e., below  $3 \text{ cm s}^{-1}$ ).

A region of strong (exceeding  $25 \text{ cm s}^{-1}$ )  $K_1$  tidal currents is evident at the shelf edge to the northwest of the Hebrides ([Fig. 4c](#) ) in the area of maximum tidal elevation. The magnitude of the  $K_1$  tidal currents reaches a maximum in the area about midway between the shelf edge and the west coast of the northern island of the Hebrides, with tidal current strength decreasing in the deep water regions to the west of the shelf edge.

A second region of enhanced shelf-edge tidal currents is evident at about  $57.5^\circ\text{N}$ . In this area the tidal currents are near circular, although their magnitude decreases and they become more rectilinear in the shallow water to the east of this. A third shelf edge region of enhanced near-circular tidal current ellipses is evident at  $56.8^\circ\text{N}$ . Although the spatial distribution of these features is similar to that found for the  $O_1$  tide, the exact location is slightly different. This is because the period of the  $K_1$  tide (23.94 h) is slightly different from the  $O_1$  tide (25.82 h), and hence resonance with the first mode shelf wave changes to a location where the topography can support a shelf wave with the  $K_1$  period.

A comparison of the semimajor axis, orientation of the ellipse, and sense of rotation of observed and computed  $O_1$  tidal currents is given in [Table 4](#) . Differences between observed and computed  $O_1$  currents at locations U, V, T, Q, P, and R are comparable with those reported in XD96 and are due to open-boundary input and errors in bottom topography.

At locations W, I, J, and K the model overpredicts the  $O_1$  tidal current by a factor of about 2, which is significantly better than the factor of 4 reported in XD96, suggesting that the enhanced resolution and use of the biharmonic viscosity has improved the accuracy of the model in this region. By using a finer horizontal grid, the local gradient of bottom topography, particularly in the shelf edge region where currents show significant spatial variability can be more accurately computed by the finite-difference method. Similarly the biharmonic form of the horizontal diffusion is more scale selective than the Laplace form and hence damps the very short physically unrealistic waves without affecting the physically realistic spatial variations that are found in the diurnal tides at the shelf edge and are artificially smoothed by the Laplacian form of horizontal viscosity.

At shallow water locations G to A, the model reproduces the semimajor axis to a higher level of accuracy than that at locations W to H, although again there are errors in the orientation of the ellipse. One reason for these large errors in orientation (of order  $90^\circ$ ), is that at locations P, Q, R, S, J, and K the current ellipse is near circular and hence it is difficult to distinguish between the major and minor axis, which readily change, with a corresponding  $90^\circ$  change in ellipse orientation in response to small model variations. Consequently, in a region of near-circular current ellipses the orientation of the major axis is not a meaningful parameter to use in assessing model accuracy.

Considering the  $K_1$  tide ([Table 5](#) ) at locations shown in [Fig. 1c](#)  (excluding location L for which a  $K_1$  analysis was not available). At locations S and R and on shelf location O, the model accurately (to on average  $1.5 \text{ cm s}^{-1}$ ) reproduces the current. Similarly, at positions N and M to the south of this, the model reproduces the current magnitude. However, farther south at locations W, I, J, K, and H the model significantly (on average by the order of  $4 \text{ cm s}^{-1}$ ) overpredicts the magnitude of the semimajor axis. This result is consistent with that found for the  $O_1$  component of the tide and suggests that this local intensification may be spurious. At shallow locations G to B the model appears to reproduce the semimajor axis, although in this region the current strength is about half that observed at locations W to H. As with the  $O_1$  tide at many

positions there are significant (of order over 90°) changes in the orientation of the current ellipse, although as discussed previously this is difficult to use as a measure of the model's accuracy in regions of near-circular tidal current.

## 1) WINTER STRATIFICATION

In a subsequent calculation (calc 2, [Table 1](#) ) input to the model was identical to that used previously, but the temperature varied in the vertical in a manner corresponding to winter stratification ([Ellett et al. 1986](#)). The essential features of the temperature profile in winter ([Fig. 1a](#) ) is a linear decrease of 1°C over the top 80 m with a subsequent decrease in temperature of a similar amount between 80 and 900 m. In the absence of a detailed synoptic density field, with a corresponding accurate current measurement dataset, and since we are primarily concerned with the influence of typical density fields upon the diurnal currents (see earlier discussion), an identical density profile was used at each horizontal grid point.

Although the  $M_2$  cotidal chart and current ellipses at the sea surface and seabed (not shown) exhibited similar spatial distributions to those found previously under homogeneous conditions, there were differences in the shelf edge region and in the oceanic regions where the water depths changed (e.g., the Anton Dohrn Seamount and Rockall Bank). The reason for these differences is that the model can now generate internal tides ([Baines 1982](#); [Craig 1987, 1988](#); [Holloway 1984](#)) as the internal density surfaces move up and down over the shelf slope in response to the tidal propagation onto and off the shelf. (Similar internal tide generation mechanisms exist associated with topographic features such as Anton Dohrn Seamount and Rockall Bank, which produce internal tides to the west of the shelf edge). Associated with these internal tides are regions of increased surface and bed currents, with the latter producing regions of increased bed friction. A detailed discussion of internal tides is beyond the scope of this paper, although as shown by [Xing and Davies \(1998a\)](#) in a comparison of a numerical solution with an inviscid analytical solution due to [Craig \(1987\)](#), if the numerical solution is going to precisely reproduce all the features of the analytic solution, then the finite-difference grid must be the order of 0.6 km. Also to reproduce this analytical solution where a constant shelf-edge slope and linear density variation were precisely known, these had to be specified exactly in the calculation. In the simulations considered here neither an accurate three-dimensional density field nor a bottom topography dataset was available on a 0.6-km grid. However, this is not a critical limitation in that, as discussed previously, the observational dataset is not synoptic or available to a high level of accuracy. Consequently for the primary aim of this paper, namely, an investigation of the effects of stratification on diurnal tides, the finite-difference grid of the model and the corresponding bottom topography and stratification should be accurate enough to enable the model to reproduce the main features of the internal tide and, hence, the influence of this and stratification effects upon the diurnal tides.

Comparing  $M_2$  tidal current ellipses ([Table 3](#) ) it is evident that at locations U to P winter stratification does not significantly influence the magnitude of the semimajor axis, although at locations R and S near the shelf edge the magnitude of the near-bottom current is reduced. However, at location L in deep water the current magnitude at all depths is increased.

At shelf edge locations N and W, stratification effects lead to a significant (of order  $4 \text{ cm s}^{-1}$ ) reduction in the current, although farther south at location K a small increase is evident. At shelf locations H to F stratification has only a small influence, although at location C situated to the north of the North Channel where tidal currents are strong and water depths change rapidly a significant (of order  $10 \text{ cm s}^{-1}$ ) reduction in near-surface current—although with a corresponding increase in near-bed current—is evident presumably due to internal tide generation in this area.

Both the  $O_1$  and  $K_1$  cotidal charts ([Figs. 6a,b](#) ) show a region of maximum tidal amplitude on the shelf edge to the northwest of the Hebrides, although the magnitude is reduced in this region compared with previously (cf. [Figs. 6a,b](#)  and [4a,b](#) ). Also the local maxima previously found in the shelf edge region to the south of this are significantly reduced for both constituents.

Comparing the spatial distribution of  $O_1$  and  $K_1$  current ellipses ([Figs. 7a,b](#)  ) with those found previously ([Figs. 5a,b](#)  ) it is evident that the spatial extent of the region of enhanced current magnitude at  $58.5^\circ\text{N}$  has been reduced. Also there is no evidence of a region of enhanced currents at the shelf edge at  $57.8^\circ\text{N}$ . Although current magnitudes increase to the south of this, the maximum found previously at  $56.6^\circ\text{N}$  is no longer present. Although there are significant changes in the shelf edge region when stratification is included, away from this area stratification has no major influence.

To quantify the effects of stratification on  $O_1$  and  $K_1$  tidal currents, it is interesting to examine the changes in the semimajor axis of the current ellipse at the locations given in [Tables 4](#)  and [5](#) . Although at sites U, V, and T there is only a small change in magnitude of the semimajor axis, at shelf edge location Q, P, S, and R there is a significant reduction in the semimajor axis when stratification effects are included (compare calcs 1 and 2), leading to an improvement between model and observations at locations Q, P, and S. A significant reduction at shelf edge locations W to H also takes place in the semimajor axis of the current ellipse ([Table 4](#)  and [5](#) , calc 2) when stratification effects are included due to the

removal of the region of local intensification found previously at 57°N. Again this leads to an improvement in the accuracy of the model.

At the shelf locations G to B, the effect of winter stratification is small.

## 2) SUMMER STRATIFICATION

The summer temperature profile used in the model (Fig. 1a) is characterized by surface temperatures decreasing by the order of 4°C over a surface layer of depth 100 m with a linear decrease by 1°C down to a water depth of 900 m.

Repeating the previous calculation, but with a temperature profile typical of summer stratification (calc 3, Table 1), gave an  $M_2$  cotidal chart in near-coastal regions similar to that found previously assuming the water to be homogeneous or with winter stratification. However, in the shelf edge region and in deeper water the smooth variation in co-amplitude and co-phase lines found under homogeneous or winter conditions does not occur (cf. Fig. 8 with Fig. 2), with the cotidal chart showing local small-scale variations, associated with internal tide generation over local topography, with enhancements of the bottom currents and hence bottom friction affecting the propagation of the surface tide.

Comparing  $M_2$  surface current ellipses computed with summer stratification (Fig. 9a) with those obtained previously (Fig. 3a), shows that tidal current ellipses in the shallower regions on the shelf exhibit similar spatial distributions to those computed previously. However, it is clear that in the shelf edge region and to the west of it, particularly in the regions of topographic change (e.g., Anton Dohrn Seamount and Rockall Bank), the surface tidal current with summer stratification is on average significantly stronger than that determined under homogeneous or winter stratified conditions. Also the spatial variability is larger since the intensity of surface currents depends upon the generation point for the internal tide and where the characteristics associated with the internal tide reach the surface.

Bed currents computed with summer stratification (Fig. 9b), although not very different from those computed previously (Fig. 3b), show regions of enhanced current with a different orientation of the major axis of the current ellipse in areas such as the shelf edge and oceanic regions of sloping seabed. In these areas internal tides can be generated with an associated increase in bottom currents. Comparing tidal current ellipses computed with winter and summer stratification (Table 3) shows that at locations U to S there are small differences (of the order of  $1 \text{ cm s}^{-1}$ ) between the semimajor axis under summer and winter conditions. At locations R, L, and N the near-bed current decreases with near-surface current increasing, giving rise to increased shear in the vertical, in better agreement with observations. At location W currents increase at all water depths, reducing the agreement with observations. An opposite effect to that found at locations R, L, and N is evident at locations I and J where the near-bed currents increase and surface currents decrease in changing from winter to summer stratification. At positions G to A, differences between summer and winter stratification are small, although at location B, the near-bed current decreases with an increase in surface current, producing an improved agreement with observations.

The variation in current [namely, decrease (increase) in near surface (bed) current] at different locations when stratification changes from winter to summer can be explained in terms of changes in the distribution of the internal tide. Cross-sectional models (Baines 1982; Craig 1987, 1988; Holloway 1994; Xing and Davies 1998a,b) show that, as the stratification changes, the internal ray paths along which internal tidal energy propagates also change, and this can lead to enhancements or reductions in near-surface/bed currents at specific locations. At the time tidal currents were measured (the observations in Table 3 were not synoptic but represent a composite from a number of observational periods) no detailed salinity and temperature survey was made that could be used in the present model. However, from previous measurements in the area (McKay et al. 1986) it is well known that there is significant horizontal spatial variability, which will influence the distribution of the internal tide. The assumption made here of applying a typical winter and summer temperature profile at each location, although useful in determining the major differences in internal tides between summer and winter, is not sufficiently accurate to enable a precise comparison with observations to be made.

The  $O_1$  and  $K_1$  cotidal charts (Figs. 10a,b), although showing similar features in shallow water to those computed assuming a homogeneous sea region (Figs. 4a,b), are significantly different in the shelfbreak region. In particular, the region of increased tidal elevation to the northwest of the Hebrides is reduced and the two areas of local intensification along the shelf slope at approximately 57.8° and 56.8°N no longer occur, with a corresponding change in the tidal phase in these regions.

The spatial distribution of surface and bed tidal current ellipses (Figs. 11a-d) is not significantly different from that found with winter stratification. A region of enhanced current magnitude exists at about 58.5°N with a similar spatial extent to that found with winter stratification. Also, there is no evidence of the regions of enhanced current magnitude to the south of this that occurred under homogeneous conditions. Current ellipses at the seabed with both summer and winter stratification showed a reduction compared with surface currents on the shelf due to frictional effects.

Comparison of observed and computed  $O_1$  ellipses (Table 4) shows that there are only minor differences (less than  $0.5 \text{ cm s}^{-1}$ ) in the magnitude of the semimajor axis computed with summer and winter stratification, although at some locations the orientation of the current ellipse changes by more than  $10^\circ$ . However, comparing the summer stratified results with those obtained under homogeneous conditions, the significant reduction in the semimajor axis at locations W, I, J, K, and H found previously with winter stratification is clearly evident. Similarly for the  $K_1$  ellipse parameters (Table 5) there are no significant differences at locations U to M. At positions W to H the reduction in the semimajor axis between assuming a homogeneous water column and that computed with summer stratification is comparable to that found previously with winter stratification, with stratification making no significant difference to current ellipses in shallow water locations (e.g., positions G to B).

This series of calculations suggests that although the seasonal stratification influences, in particular the magnitude of the surface  $M_2$  tidal current ellipse by producing a surface-enhanced internal tide in summer, it is the stratification at depth that has an influence upon the  $O_1$  and  $K_1$  tidal currents in the shelf edge region. These tidal constituents have a number of regions along the shelf edge of enhanced current magnitude under homogeneous conditions that are reduced to one region when stratification is included. By considering two diurnal tidal constituents, namely  $O_1$  with a period of 25.82 h ( $13.94^\circ/\text{h}$ ) and  $K_1$  with a period of 23.94 h ( $15.04^\circ/\text{h}$ ), we have shown that the grid resolution of the model is sufficiently fine to represent local changes in shelf edge topography with the necessary accuracy to represent the observed slight differences in location of regions of local intensification of these constituents. Also that including stratification improves the agreement between observed and computed tidal currents for both tidal constituents is more conclusive than if comparisons were made for a single constituent.

Comparing surface and bottom current ellipse distributions (Figs. 13a,b), it is clear that although the spatial distributions are comparable, bottom friction has reduced the magnitude of the currents to a similar extent to that found previously for the  $O_1$  tide.

#### 4. Frictional influence (a hybrid 2D/3D model calculation)

In the previous series of calculations the spatial distribution of the  $O_1$  and  $K_1$  tidal currents under both homogeneous and stratified conditions was examined in detail using the three-dimensional model. Under homogeneous conditions the diurnal tidal currents exhibited spurious intensification in certain shelf edge regions, which was not found when stratification effects were included. This result suggests that it is crucial to include stratification effects, a finding that is at variance with calculations performed using vertically integrated two-dimensional models (Flather 1988; Foreman et al. 1993), which cannot include stratification effects yet appear (Foreman et al. 1993) to reproduce the diurnal tidal currents.

In this section we consider if the hybrid 2D/3D model in which the water is assumed to be homogeneous and bottom friction is computed from the depth-mean current (in essence, a two-dimensional model that also predicts current profiles) can produce the main features of the diurnal tides at the shelf edge.

In this two-dimensional calculation (calc 4, Table 1) the tidal input to the model was identical to that used previously (calc 1, Table 1), although the bed stress was computed from the depth-mean current with an appropriate 2D friction coefficient  $k = 0.003$ .

The computed  $M_2$  co-tidal chart was indistinguishable from that found previously, and a comparison of observed and computed amplitude and phase of the  $M_2$  tide at a number of coastal and offshore tide gauge (calc 4, Table 2a) did not reveal any significant differences between calcs 4 and 1, although the rms errors were slightly worse (calc 4 gave rms errors of 12.4 cm and  $18.0^\circ$ , with calc 1 giving 8.4 cm and  $16.5^\circ$ ). Also no significant differences were found in the  $M_2$  tidal current ellipses.

However, there were significant differences in the diurnal tides, which we will illustrate here with reference to the  $O_1$  tide since this has been examined previously (Proctor and Davies 1996; XD 96) in detail with lower-resolution models.

The  $O_1$  cotidal chart (Fig. 12) however showed a reduction in the magnitude of the  $O_1$  tide to the northwest of the Hebrides, with a reduction at the other shelf edge locations to the south of this (cf. Fig. 12 and Fig. 4a). Also some changes to the co-phase lines are evident in the region to the northwest of the Hebrides (cf. Fig. 12 and Fig. 4a). Comparing  $O_1$  tidal elevations and phases computed with the two-dimensional model with those obtained previously and from measurements (Table 2b, calc 4) it is evident that the differences between the “hybrid” model and three-

dimensional model are small, with a slight change to the rms error (calc 4 gave rms errors of 1.8 cm and 14.5°, compared to calc 1, rms errors of 1.9 cm and 17.2°).

Although the changes in tidal elevation, amplitude, and phase are small, it is evident from a comparison of surface and bed current ellipses (Figs. 13a,b) computed with the hybrid 2D/3D model to those obtained previously under homogeneous conditions (Figs. 5a,b) that the magnitude of the  $O_1$  currents to the northwest of the Hebrides has been reduced, with a decrease of  $O_1$  tidal currents at the shelf edge at 57.5° and 56.6°N. Although using a two-dimensional formulation of bottom friction in the three-dimensional model (the hybrid 2D/3D model) has reduced the magnitudes of the  $O_1$  currents compared to those computed with the three-dimensional model, due to enhanced friction, it is clear that the areas of local enhancement—although with reduced current magnitude—still occur at 57.5° and 56.6°N and that the spatial distribution of currents resembles those found in the full three-dimensional homogeneous model (all be it with reduced amplitude) rather than those found with stratification effects included (Figs. 7a,b; Figs. 11a,b).

The reduction in the semimajor axis of the  $O_1$  tidal current ellipse due to the additional friction produced by relating the bed stress to the depth-mean current is clearly evident from Table 4 (cf. calc 4 with calc 1), particularly at locations W, I, J, K, and H where the semimajor axis has decreased from about 7 cm s<sup>-1</sup> (calc 1) to approximately 4 cm s<sup>-1</sup> (calc 4), a change comparable to that due to stratification effects.

Based purely upon the limited set of observations shown in Table 4, it would appear that enhancing bottom friction or including stratification effects has similar results, namely, improving the accuracy of modeled and observed currents, in particular by reducing the magnitude of the semimajor axis of the current ellipse at locations W to H. However, it is clear from the spatial distribution of the  $O_1$  current ellipses that stratification effects change their spatial distribution, whereas increasing friction reduces their magnitude. In terms of the  $O_1$  cotidal chart, although tidal elevation amplitudes and phases are influenced by stratification and frictional effects, the dominant influence is the shelf wave resonance. Consequently cotidal charts can be determined using a conventional two-dimensional model, or a three-dimensional model assuming a homogeneous sea region. However, the spatial distribution of currents is more sensitive and requires the influence of stratification effects.

## 5. Concluding remarks

In this paper we have briefly outlined the major steps in developing a three-dimensional hydrodynamic model of the shelf edge region to the west of Scotland. The model uses a staggered finite-difference grid in the horizontal, with a one time level integration scheme and the total variation diminishing scheme for density advection to solve the equations. The finite-difference grid is significantly finer than that used in previous models of the region (Proctor and Davies 1996; XD96).

A turbulence energy scheme has been used in the vertical to parameterize the subgrid-scale mixing, with biharmonic friction in the horizontal. Calculations are performed to examine the spatial variability of  $M_2$ ,  $O_1$ , and  $K_1$  tidal elevations and currents in the area and the influence of idealized stratification (both winter and summer) upon the tides in the region. Unlike previous calculations where stratification effects were included in a diagnostic manner (XD96), stratification was included in a prognostic manner and hence internal tides were generated as the internal pressure gradients evolved with time.

Although  $M_2$  tidal elevations were not significantly influenced by stratification effects, tidal currents were, particularly when summer stratification was included that produced major changes in the intensity of surface tidal currents due to the generation of internal tides.

The spatial distribution of the  $O_1$  tidal elevations and currents under homogeneous conditions was not significantly different from that computed previously (XD96) with a coarser-grid model of the region and showed a number of regions along the shelf edge where the  $O_1$  tidal current was significantly larger than the observed. Local intensification of the diurnal tides at the shelf edge can be expected from theory, as a resonance with the shelf wave in the area, and the homogeneous model appears to correctly reproduce this in the region to the northwest of the Hebrides, although the local intensifications to the south of this were not supported by the observations, suggesting that they were spurious. However, when stratification effects (either winter or summer) were included, these spurious local intensifications were removed.

The model was also used to examine the influence of stratification on the  $K_1$  tide in the region. As for the  $O_1$  tide, local intensification due to a shelf wave resonance occurs with the  $K_1$  tide in the shelf edge region although under homogeneous conditions some spurious enhancements are found, which are removed when stratification effects are included.

The role of stratification in determining the spatial distribution of the diurnal tides in the shelf edge region off the west

coast of Scotland appears rather complex. Without stratification effects or when it is included diagnostically (XD96), regions of local enhancement appear that are not supported by observations. With stratification these areas are removed, possibly because the form and period of the shelf wave changes when stratification is included, which affects the resonance with the diurnal tidal in such a manner as to remove the regions of spurious enhancement due to resonance. An alternative is that changes in friction due to the effect of stratification also affect the resonance in such a manner as to remove the regions of spurious enhancement. The calculations with the hybrid model clearly show that frictional effects, both bottom and internal, influence the local enhancement of the diurnal tide, although the spatial distributions of the currents are different. This helps to explain why two-dimensional models, which cannot include vertical stratification effects, can still reproduce the observed spatial distributions of tidal elevations. However, when stratification effects are neglected in three-dimensional models, they fail to reproduce the detailed distribution of diurnal tidal currents that are only reproduced when stratification effects are included.

### Acknowledgments

The authors are indebted to Mr. R. A. Smith for help in preparing figures and Mrs. L. Parry and Mrs. L. Ravera for typing the paper.

---

### REFERENCES

- Abraham, G., and H. Gerritsen, 1990: Sub-grid transport of matter in two-dimensional tidal flow over an uneven bed. *Contin. Shelf Res.*, **10**, 225–242..
- Baines, P. G., 1982: On internal tide generation models. *Deep-Sea Res.*, **29**, 307–338..
- Baumert, H., and G. Radach, 1992: Hysteresis of turbulent kinetic energy in nonrotational tidal flows: A model study. *J. Geophys. Res.*, **97**, 3669–3677..
- Blumberg, A. F., and G. L. Mellor, 1987: A description of a three-dimensional coastal ocean circulation model. *Three-Dimensional Coastal Ocean Models*, N. S. Heaps, Ed., *Coastal and Estuarine Sciences*, No. 4, Amer. Geophys. Union, 1–16..
- Craig, P. D., 1987: Solutions for internal tidal generation over coastal topography. *J. Mar. Res.*, **45**, 83–105..
- , 1988: A numerical model study of internal tides on the Australian Northwest Shelf. *J. Mar. Res.*, **46**, 59–76..
- Davies, A. M., 1987: Spectral models in continental shelf sea oceanography. *Three-Dimensional Coastal Ocean Models*, N. S. Heaps, Ed., Amer. Geophys. Union, 71–106..
- , and H. Gerritsen, 1994: An intercomparison of three-dimensional tidal hydrodynamic models of the Irish Sea. *Tellus*, **46A**(2), 200–221..
- , and J. Xing, 1995: An intercomparison and validation of a range of turbulence energy schemes used in three dimensional tidal models. *Qualitative Skill Assessment for Coastal Ocean Models*, D. R. Lynch and A. M. Davies, Eds., Coastal and Estuarine Series, No. 47, Amer. Geophys. Union, 71–96..
- , J. E. Jones, and J. Xing, 1997a: A review of recent developments in tidal hydrodynamic modelling. Part 1. Spectral models. *J. Hydrol. Eng. ASCE*, **123** (4), 278–292..
- , —, and —, 1997b: A review of recent developments in tidal hydrodynamic modelling. Part 2. Turbulence energy models. *J. Hydrol. Eng. ASCE*, **123** (4), 293–302..
- Ellett, D. J., A. Edwards, and R. Bowers, 1986: The hydrography of the Rockall Channel—An overview. *The Oceanography of the Rockall Channel*, *Proc. Roy. Soc. Edinburgh*, **88B**, 61–81..
- Flather, R. A., 1988: A numerical model investigation of tides and diurnal-period continental shelf waves along Vancouver Island. *J. Phys. Oceanogr.*, **18**, 115–139..
- Foreman, M. G. G., R. F. Henry, R. A. Walters, and V. A. Ballantyne, 1993: A finite element model for tides and resonance along the north coast of British Columbia. *J. Geophys. Res.*, **98**, 2509–2531..
- Galperin, B., L. H. Kantha, S. Hassid, and A. Rosati, 1988: A quasi-equilibrium turbulent energy model for geophysical flows. *J. Atmos. Sci.*, **45**, 55–62.. [Find this article online](#)
- , A. Rosati, L. H. Kantha, and G. L. Mellor, 1989: Modelling rotating stratified turbulent flows with application to oceanic mixed

layers. *J. Geophys. Res.*, **94**, 901–916..

Greenberg, D. A., 1990: The contribution of modelling to understanding the dynamics of the Bay of Fundy and the Gulf of Maine. *Modelling Marine Systems*, A. M. Davies, Ed., Vol. 2, CRC Press, 107–140..

Heathershaw, A. D., J. Small, and C. E. Stretch, 1994: Frictional formulations in numerical ocean models and their effect on simulated acoustic fields. *J. Phys. Oceanogr.*, **24**, 274–297..

Holloway, P. E., 1984: On the semi-diurnal internal tide at a shelf-break region on the Australian north-west shelf. *J. Phys. Oceanogr.*, **14**, 1778–1790..

—, 1996: A numerical model of internal tides with application to the Australian North West Shelf. *J. Phys. Oceanogr.*, **26**, 21–37..

Huthnance, J. M., 1989: Internal tides and waves near the continental shelf edge. *Geophys. Astrophys. Fluid Dyn.*, **48**, 81–105..

Huthnance, J. M. and P. G. Baines, 1982: Tidal currents in the north west Africa upwelling region. *Deep-Sea Res.*, **19**, 285–306..

Lamb, K. G., 1994: Numerical experiments of internal wave generation by strong tidal flow across a finite amplitude bank edge. *J. Geophys. Res.*, **99**, 843–864..

Le Provost, C., M. L. Genco, and F. Lyard, 1995: Modelling and predicting tides over the World Ocean. *Quantitative Skill Assessment for Coastal Ocean Models*, D. R. Lynch and A. M. Davies, Eds., No. 47, Amer. Geophys. Union, Coastal and Estuarine Series, 175–202..

Luyten, P. J., 1995: An analytical and numerical study of surface and bottom boundary layers with variable forcing and application to the North Sea. *J. Mar. Syst.*, **8**, 171–190..

—, E. L. Deleersnijder, K. G. Ruddick, and J. Ozer, 1996: Presentation of a family of turbulence closure models for stratified shallow water flows and preliminary application to the Rhine outflow region. *Contin. Shelf Res.*, **16**, 101–130..

Lynch, D. R., and C. E. Naimie, 1993: The  $M_2$  tide and its residual on the outer banks of the Gulf of Maine. *J. Phys. Oceanogr.*, **23**, 2222–2253..

Martinsen, E. A., and H. Engedahl, 1987: Implementation and testing of a lateral boundary scheme as an open boundary condition in a barotropic ocean model. *Coastal Eng.*, **11**, 603–627..

McKay, W. A., M. S. Baxter, D. J. Ellett, and D. T. Meldrum, 1986: Radiocaesium and circulation patterns west of Scotland. *J. Environ. Radioact.*, **4**, 205–232..

New, A. L., 1988: Internal tidal mixing in the Bay of Biscay. *Deep-Sea Res.*, **35**, 691–709..

—, and R. D. Pingree, 1990: Evidence for internal tidal mixing near the shelf break in the Bay of Biscay. *Deep-Sea Res.*, **37**, 1783–1803..

Oey, L.-Y., and P. Chen, 1992: A nested-grid ocean model: With application for the simulation of meanders and eddies in the Norwegian coastal current. *J. Geophys. Res.*, **97**, 20 063–20 086..

Owen, A., 1980: A three-dimensional model of the Bristol Channel. *J. Phys. Oceanogr.*, **10**, 1290–1302..

Proctor, R., and A. M. Davies, 1996: A three dimensional model of tides off the north-west coast of Scotland. *J. Mar. Syst.*, **7**, 43–66..

Pugh, D. T., and J. M. Vassie, 1976: Tide and surge propagation offshore in the Dowing Region of the North Sea. *Dtsch. Hydrogr. Z.*, **29**, 163–213..

Sherwin, T. J., 1988: Analysis of an internal tide observed on the Malin shelf, north of Ireland. *J. Phys. Oceanogr.*, **18**, 1035–1050..

—, 1991: Evidence of a deep internal tide in the Faeroe–Shetland Channel. *Tidal Hydrodynamics*, B. B. Parker, Ed., John Wiley and Sons, 469–488..

Spaulding, M. L., 1984: A vertically averaged circulation model using boundary fitted coordinates. *J. Phys. Oceanogr.*, **14**, 973–982..

Xing, J., and A. M. Davies, 1996a: Determination of tidal currents on the Malin–Hebrides shelf using a three dimensional hydrodynamic model with turbulence closure. *J. Phys. Oceanogr.*, **26**, 417–447..

—, and —, 1996b: The influence of mixing length formulation and stratification upon tidal currents in shallow seas. *Estuarine, Coastal Shelf Sci.*, **42**, 417–456..

—, and —, 1996c: Application of a range of turbulence energy models to the determination of  $M_4$  tidal current profiles. *Contin. Shelf*

— ,and — ,1998a: Formulation of a three-dimensional shelf edge model and its application to internal tide generations. *Contin. Shelf Res.*, in press..

— ,and — ,1998b: Application of a range of turbulence energy models to the computation of the internal tide. *Int. J. Numer. Methods Fluids*, 26, 1055–1084..

### Tables

Table 1. Summary of parameters used in the calculations.

Calculation	Stratification
1	Homogeneous
2	Winter
3	Summer
4	Homogeneous 2D/3D model

[Click on thumbnail for full-sized image.](#)

Table 2a. Comparison of computed and observed  $M_2$  elevation tidal amplitude  $h$  (cm) and phase  $g$  (deg) at a number of coastal and offshore locations.

Locn	Obs		Calc 1		Error		Calc 4		Error	
	$h$	$g$	$h$	$g$	$\Delta h$	$\Delta g$	$h$	$g$	$\Delta h$	$\Delta g$
1	104	191	94	200	-10	9	90	200	-11	9
2	140	208	141	217	1	9	140	217	-1	9
3	119	190	114	199	-5	9	113	199	-6	9
4	136	197	130	206	-6	9	130	207	-6	10
5	96	176	90	182	-6	7	90	182	-6	7
6	106	178	100	186	-6	8	100	186	-6	8
7	140	193	132	204	-8	11	132	205	-8	12
8	107	170	104	183	-3	13	104	183	-3	13
9	129	185	125	191	-4	6	125	192	-4	7
10	146	199	144	208	-2	9	143	208	-3	9
11	130	177	121	185	-9	8	121	187	-9	10
12	133	185	131	192	-2	7	130	193	-3	8
13	110	180	106	185	-4	5	106	187	-4	7
14	102	168	97	175	-5	7	97	175	-5	7
15	101	168	97	174	-4	6	97	175	-4	7
16	105	168	101	174	-4	6	101	175	-4	7
17	118	171	117	177	-1	6	116	178	-2	7
18	136	195	132	202	-4	7	131	203	-5	8
19	109	168	107	174	-2	6	106	175	-3	7
20	113	233	118	177	5	-55	117	179	4	-53
21	118	166	121	170	3	-4	121	172	3	-6
22	114	165	116	162	2	-3	116	164	2	-1
23	113	163	100	159	-13	-4	102	162	-11	-1
24	65	135	97	158	32	23	99	162	34	27
25	106	163	100	163	-6	0	102	165	-4	2
26	112	163	107	170	-5	7	108	171	-4	8
27	107	163	105	160	-2	-4	106	163	-1	-3
28	104	159	100	166	-4	7	100	166	-4	7
29	107	157	102	164	-5	7	102	164	-5	7
30	97	198	93	201	-4	3	93	197	-4	-11
31	108	178	107	184	-1	6	111	181	3	3
32	97	175	91	184	-6	9	96	181	-1	6
33	16	92	21	129	5	37	21	131	5	39
34	10	81	32	127	22	46	32	127	22	46
35	107	162	96	168	-11	6	96	168	-11	6
36	109	160	96	161	-13	1	96	161	-13	0
37	109	160	96	161	-13	1	96	161	-13	0
38	7	125	16	168	9	43	16	168	9	43
39	43	309	32	300	-11	-9	32	289	-21	-20
40	6	237	6	237	0	0	6	237	0	0
41	105	160	93	169	-12	9	93	169	-12	10

[Click on thumbnail for full-sized image.](#)

Table 2b. Comparison of computed and observed  $O_1$  elevation tidal amplitude  $h$  (cm) and phase  $g$  (deg) at a number of coastal and offshore locations.

Location	Obs		Calc 1		Error		Calc 4		Error	
	$h$	$g$	$h$	$g$	$\Delta h$	$\Delta g$	$h$	$g$	$\Delta h$	$\Delta g$
1	8	4	7	20	-2	16	7	15	-1	11
2	8	305	8	337	0	-13	7	347	-1	-13
3	6	331	8	334	2	-7	8	331	2	0
4	9	356	8	355	-1	5	8	358	-1	2
5	8	4	7	16	-1	12	7	15	-1	11
6	7	267	6	262	-1	5	6	264	-1	7
7	9	349	8	358	-2	9	8	357	-1	12
8	7	353	6	352	-1	1	6	353	-1	6
9	6	10	3	340	-3	-30	4	346	-2	-24
10	8	344	7	341	-1	-4	7	345	-1	1
11	3	353	4	310	0	-43	4	327	1	-26
12	9	303	6	343	-3	13	6	354	-3	24
13	7	15	5	18	-2	3	6	16	1	1
14	7	356	7	1	0	5	7	1	0	5
15	7	357	7	1	-1	4	7	1	-1	4
16	7	359	7	1	-1	1	7	1	-1	1
17	3	16	3	16	0	0	3	10	0	-6
18	8	307	6	343	-2	-9	6	304	-2	3
19	6	3	6	1	0	-2	6	0	0	-3
20	7	44	5	43	-2	-1	5	27	-2	-13
21	5	29	4	33	-1	4	4	26	-1	-3
22	5	34	4	30	-1	16	5	41	0	7
23	8	351	5	33	-3	62	5	45	-3	54
24	7	44	5	32	-2	8	5	44	-2	0
25	8	16	5	49	-3	33	5	41	-3	25
26	7	331	6	31	-1	10	6	31	-1	10
27	5	35	5	47	0	22	5	39	0	14
28	6	355	6	356	0	1	6	355	0	0
29	6	355	6	333	0	-2	6	333	0	-2
30	8	30	6	38	-2	8	6	37	-2	7
31	8	15	6	29	-2	14	6	25	-2	10
32	7	356	6	31	-1	35	6	27	-1	33
33	8	43	6	30	-2	7	6	49	-2	7
34	8	37	6	32	-2	15	6	39	-2	13
35	10	44	7	32	-3	8	7	55	-3	11
36	11	37	7	32	-4	15	7	54	-4	13
38	7	44	6	47	-1	3	6	46	-1	2
39	8	37	7	42	-1	5	7	42	-1	5
40	9	54	7	51	-2	-3	7	53	-2	-1
41	1	40	7	51	6	11	7	53	6	13

[Click on thumbnail for full-sized image.](#)

Table 2c. Comparison of computed and observed  $K_1$  elevation tidal amplitude  $h$  (cm) and phase  $g$  (deg) at a number of coastal and offshore locations.

Location	Obs		Calc 1		Error		Calc 4		Error	
	$h$	$g$	$h$	$g$	$\Delta h$	$\Delta g$	$h$	$g$	$\Delta h$	$\Delta g$
1	8	4	7	20	-2	16	7	15	-1	11
2	8	305	8	337	0	-13	7	347	-1	-13
3	6	331	8	334	2	-7	8	331	2	0
4	9	356	8	355	-1	5	8	358	-1	2
5	8	4	7	16	-1	12	7	15	-1	11
6	7	267	6	262	-1	5	6	264	-1	7
7	9	349	8	358	-2	9	8	357	-1	12
8	7	353	6	352	-1	1	6	353	-1	6
9	6	10	3	340	-3	-30	4	346	-2	-24
10	8	344	7	341	-1	-4	7	345	-1	1
11	3	353	4	310	0	-43	4	327	1	-26
12	9	303	6	343	-3	13	6	354	-3	24
13	7	15	5	18	-2	3	6	16	1	1
14	7	356	7	1	0	5	7	1	0	5
15	7	357	7	1	-1	4	7	1	-1	4
16	7	359	7	1	-1	1	7	1	-1	1
17	3	16	3	16	0	0	3	10	0	-6
18	8	307	6	343	-2	-9	6	304	-2	3
19	6	3	6	1	0	-2	6	0	0	-3
20	7	44	5	43	-2	-1	5	27	-2	-13
21	5	29	4	33	-1	4	4	26	-1	-3
22	5	34	4	30	-1	16	5	41	0	7
23	8	351	5	33	-3	62	5	45	-3	54
24	7	44	5	32	-2	8	5	44	-2	0
25	8	16	5	49	-3	33	5	41	-3	25
26	7	331	6	31	-1	10	6	31	-1	10
27	5	35	5	47	0	22	5	39	0	14
28	6	355	6	356	0	1	6	355	0	0
29	6	355	6	333	0	-2	6	333	0	-2
30	8	30	6	38	-2	8	6	37	-2	7
31	8	15	6	29	-2	14	6	25	-2	10
32	7	356	6	31	-1	35	6	27	-1	33
33	8	43	6	30	-2	7	6	49	-2	7
34	8	37	6	32	-2	15	6	39	-2	13
35	10	44	7	32	-3	8	7	55	-3	11
36	11	37	7	32	-4	15	7	54	-4	13
38	7	44	6	47	-1	3	6	46	-1	2
39	8	37	7	42	-1	5	7	42	-1	5
40	9	54	7	51	-2	-3	7	53	-2	-1
41	1	40	7	51	6	11	7	53	6	13

				135		
15	10	123	10	134	0	12
16	11	123	10	134	0	12
17	4	156	4	149	0	-8
18	9	133	9	125	0	-8
19	8	129	9	134	1	6
20	11	204	7	163	-4	-41
21	7	188	6	160	-1	-28
22	7	192	6	174	0	-18
23	4	166	7	178	3	12
24	11	182	7	177	-3	-5
25	9	174	7	174	-2	0
26	8	127	9	135	1	8
27	6	177	7	172	1	-5
28	10	113	9	129	-1	17
29	9	109	9	127	-1	18
30	9	183	9	166	0	-17
31	9	157	9	155	0	-2
32	10	171	9	158	-1	-13
33	9	188	9	179	0	-8
34	9	201	9	181	0	-20
35	11	190	11	183	0	-7
37	12	195	11	183	-1	-12
38	10	183	9	176	0	-7
39	10	182	10	171	0	-11
40	6	195	10	182	4	-13
41	12	183	11	182	-1	-1

Click on thumbnail for full-sized image.

Table 3. Comparison of observed and computed semimajor axis  $A$  (cm s<sup>-1</sup>), orientation  $\theta$  (deg), and rotation  $R$  of the  $M_2$  current ellipse at a number of depths and locations.

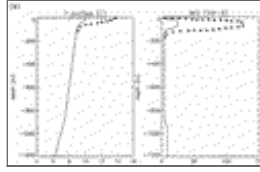
Sig	Observed			Obs 1			Obs 2			Obs 3			z(h)	zθ
	A	θ	R	A	θ	R	A	θ	R	A	θ	R		
U	23.0	163	-	19.9	156	+	19.5	156	+	18.9	156	+	110	-0.77
V	17.2	32	-	17.7	31	+	17.3	31	+	19.9	31	+	114	-0.60
T	14.3	63	+	20.9	67	-	19.6	61	+	23.2	61	+	142	-0.82
Y	15.0	76	+	18.7	74	-	18.9	75	-	18.8	75	-	142	-0.67
Q	15.2	57	-	20.9	61	-	19.4	53	-	18.0	57	-	177	-0.86
F	20.2	60	-	17.8	61	-	18.3	61	-	16.6	57	-	194	-0.22
S	14.1	55	-	22.0	62	-	20.7	58	-	21.2	55	-	146	-0.83
S	15.4	55	-	22.2	63	-	20.8	59	-	20.2	57	-	142	-0.80
S	15.0	73	-	19.1	68	-	19.5	68	-	20.2	70	-	146	-0.28
R	15.3	40	-	21.7	41	-	20.1	36	-	17.5	37	-	155	-0.84
R	16.4	59	-	18.8	67	-	19.2	67	-	21.3	67	-	152	-0.34
R	17.0	71	-	18.8	67	-	19.2	67	-	21.2	67	-	155	-0.35
O	14.7	50	+	20.4	61	+	18.6	55	+	21.0	55	+	135	-0.81
O	15.7	69	-	17.2	64	+	17.2	65	+	17.1	65	+	135	-0.44
L	8.4	71	-	10.1	78	-	14.3	101	-	12.7	106	-	589	-0.92
L	8.3	76	-	13.0	81	-	18.7	101	-	16.8	99	-	589	-0.93
L	11.9	86	-	13.0	80	-	16.4	75	-	17.6	75	-	589	-0.49
N	16.5	37	-	23.8	37	-	19.7	31	-	17.6	40	-	145	-0.83
N	16.7	51	-	22.8	43	-	19.6	42	-	17.7	48	-	145	-0.86
M	8.7	82	+	7.5	80	+	5.1	79	+	3.0	109	+	1614	-0.69
M	8.3	98	+	7.1	90	+	8.3	83	+	7.4	77	+	1614	-0.21
M	8.0	98	+	7.1	90	+	8.3	83	+	7.0	79	+	1614	-0.32
W	20	98	+	21.6	99	+	19.8	98	+	26.2	99	+	140	-0.82
W	19.2	33	-	21.0	29	-	19.8	38	-	20.4	38	-	134	-0.99
W	20.5	31	-	21.6	28	-	19.8	38	-	20.4	38	-	134	-0.99
I	19.8	25	-	18.8	35	-	17.9	34	-	20.1	45	-	134	-0.27
I	25.8	25	-	15.9	33	-	15.8	47	-	22.4	58	-	134	-0.25
J	20.8	21	-	18.0	31	-	19.2	31	-	22.3	41	-	139	-0.82
K	24.4	28	-	12.5	38	-	14.3	40	-	10.1	35	-	138	-0.35
K	19.4	23	-	13.4	34	-	16.7	36	-	16.9	37	-	138	-0.66
H	17.4	23	-	18.7	31	-	18.7	25	-	11.5	1	-	138	-0.80
H	16.2	23	-	11.5	48	-	11.7	45	-	11.5	45	-	139	-0.21
G	13.8	26	-	11.2	47	-	11.0	45	-	11.7	40	-	170	-0.18
G	14.2	23	-	11.5	48	-	11.7	45	-	11.5	45	-	139	-0.21
F	74.6	70	-	68.5	75	-	72.2	82	-	71.7	81	-	44	-0.75
C	90.5	150	-	83.1	136	-	95.1	145	-	82.6	136	-	58	-0.36
C	90.0	146	-	111.1	149	-	99.5	145	-	100.1	144	-	58	-0.36
C	90.0	149	-	111.1	149	-	99.5	145	-	100.1	144	-	58	-0.36
A	14.4	107	-	20.5	180	-	18.1	166	-	19.0	164	-	73	-0.86
A	17.6	9	-	13.3	180	-	18.1	166	-	19.0	164	-	73	-0.86
D	53.7	149	+	32.3	131	+	38.9	142	+	33.7	127	+	110	-0.95
B	34.4	13	-	48.3	137	-	42.5	6	-	42.9	170	-	54	-0.80
B	45.6	8	-	49.8	9	-	44.2	5	-	48.3	9	-	54	-0.48
B	47.8	12	-	49.9	9	-	44.7	5	-	48.8	9	-	54	-0.44

Click on thumbnail for full-sized image.

Table 4. Comparison of observed and computed semimajor axis  $A$  (cm s<sup>-1</sup>), orientation  $\theta$  (deg), and rotation  $R$  of the  $O_1$  tidal current ellipse at a number of depths and locations.

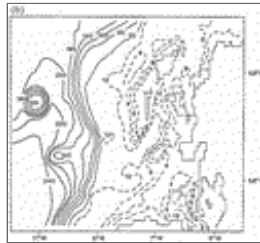
Sig	Observed			Obs 1			Obs 2			Obs 3			Obs 4			z(h)	zθ
	A	θ	R	A	θ	R	A	θ	R	A	θ	R	A	θ	R		
U	5.9	32	-	20.5	97	-	20.1	98	-	21.6	103	-	14.4	88	-	110	-0.77
V	3.2	17	-	21.0	100	-	21.0	99	-	17.9	8	-	1.6	175	-	114	-0.60
T	4.0	34	-	8.3	20	-	7.4	25	-	6.5	20	-	6.3	20	-	142	-0.82
Y	4.6	42	-	7.5	39	-	6.7	20	-	6.6	19	-	5.7	25	-	142	-0.67
Q	2.6	35	-	6.9	124	-	5.9	114	-	2.8	105	-	3.2	129	-	177	-0.86
F	3.1	2	-	7.1	133	-	6.3	120	-	6.4	119	-	5.2	122	-	194	-0.22
S	3.5	41	-	4.9	149	-	2.8	159	+	2.3	147	+	2.6	166	+	146	-0.83
S	2.6	39	-	5.5	141	-	2.8	148	+	2.3	152	+	2.5	155	+	142	-0.80
S	3.2	27	-	4.4	147	-	2.4	158	+	2.2	167	+	2.4	166	+	146	-0.28
R	3.3	49	-	4.0	100	-	1.9	118	-	1.6	96	-	2.0	116	-	155	-0.84
R	3.6	36	-	3.9	119	-	1.4	110	-	1.5	93	-	1.8	119	-	152	-0.34
R	3.7	49	-	3.9	119	-	1.4	110	-	1.5	92	-	1.8	119	-	155	-0.35
O	3.7	78	-	5.6	68	+	5.8	76	+	5.1	75	+	4.7	72	+	135	-0.81
O	4.3	77	-	4.8	68	+	4.7	71	+	4.6	70	+	4.2	73	+	135	-0.64
L	1.4	3	-	2.0	88	-	6.0	38	-	6.0	26	-	1.9	88	-	589	-0.92
L	1.7	177	-	2.5	68	-	6.5	35	-	6.4	42	-	2.2	72	-	589	-0.83
L	1.1	10	-	2.5	81	-	4.9	102	-	4.8	100	-	2.2	82	-	589	-0.49
N	3.1	98	-	3.1	20	-	4.0	110	-	4.4	112	-	1.4	77	-	145	-0.83
N	2.6	9	-	3.1	20	-	4.0	110	-	4.4	112	-	1.4	77	-	145	-0.83
M	0.6	107	+	0.8	158	+	1.1	79	+	1.1	95	+	0.6	133	+	1614	-0.69
M	0.3	9	-	0.8	158	+	0.8	49	+	0.7	53	+	0.6	133	+	1614	-0.13
M	0.3	72	+	0.8	158	+	0.8	20	+	0.8	35	+	0.6	133	+	1614	-0.13
W	3.6	177	-	7.1	107	-	5.6	107	-	5.0	114	-	4.4	144	-	140	-0.46
W	3.3	109	-	6.6	101	-	4.7	102	-	3.9	103	-	4.1	141	-	134	-0.79
I	3.6	100	-	7.6	30	-	5.3	104	-	2.8	111	-	4.1	146	-	134	-0.27
I	3.7	75	-	6.7	24	-	3.1	96	-	2.6	99	-	3.7	157	-	134	-0.27
J	3.6	100	-	9.0	24	-	6.0	103	-	3.7	101	-	4.9	158	-	139	-0.82
J	3.2	125	-	7.8	15	-	3.4	98	-	3.0	92	-	4.4	147	-	139	-0.32
K	4.7	107	-	6.7	16	-	2.8	99	-	2.2	87	-	3.7	146	-	138	-0.35
K	4.5	106	-	7.7	25	-	2.8	98	-	2.5	88	-	4.0	176	-	138	-0.86
H	3.9	106	-	8.4	115	-	3.4	105	-	2.8	94	-	6.3	106	-	136	-0.80
O	4.1	116	-	3.7	89	-	2.9	95	-	2.6	84	-	3.2	99	-	170	-0.71
O	3.6	114	-	3.6	89	-	2.8	96	-	3.0	103	-	3.2	99	-	170	-0.18
B	3.2	81	-	4.1	65	-	3.4	76	-	3.6	76	-	3.5	75	-	136	-0.82
P	2.3	80	-	2.5	92	-	3.3	84	-	2.2	83	-	2.1	86	-	44	-0.79
C	3.1	152	-	2.6	136	-	3.0	139	-	2.4	140	-	2.7	137	-	58	-0.81
C	3.7	152	-	3.1	136	-	3.3	137	-	3.3	138	-	3.9	135	-	58	-0.36
C	3.1	158	-	2.9	134	-	3.3	137	-	3.6	138	-	3.9	133	-	58	-0.33
A	1.5	70	-	3.4	50	-	3.5	60	-	3.0	61	-	3.2	53	-	73	-0.86
A	2.5	101	-	3.3	47	-	2.6	54	-	2.5	52	-	2.9	50	-	73	-0.44
D	1.9	126	-	1.2	174	-	1.2	164	-	1.1</							

## Figures



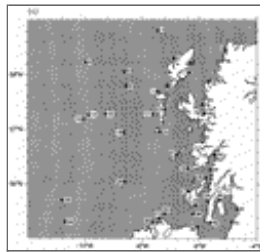
[Click on thumbnail for full-sized image.](#)

Fig. 1a. Typical winter (solid) and summer (dotted) temperature and buoyancy frequency profiles used in the calculations.



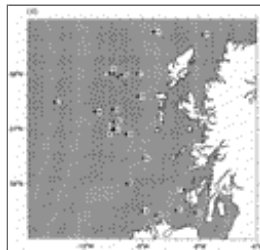
[Click on thumbnail for full-sized image.](#)

Fig. 1b. Bottom topography used in the model (all depths in units of 10 m, e.g., the 100 contour corresponds to a depth of 1000 m).



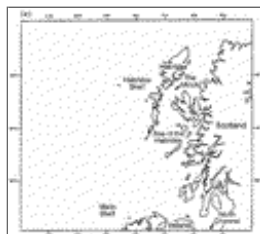
[Click on thumbnail for full-sized image.](#)

Fig. 1c. The finite-difference grid of the Malin-Hebrides model, showing the location of tide gauges used in the comparison.



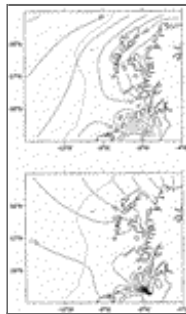
[Click on thumbnail for full-sized image.](#)

Fig. 1d. As in [Fig. 1c](#) but showing location of current meters used in the comparison.



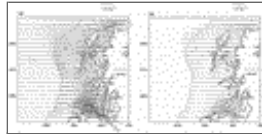
[Click on thumbnail for full-sized image.](#)

Fig. 1e. Geographical location of various regions.



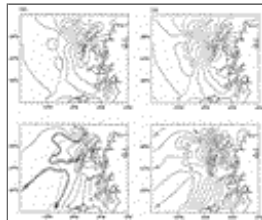
[Click on thumbnail for full-sized image.](#)

Fig. 2. Computed  $M_2$  cotidal chart, assuming a homogeneous sea region.



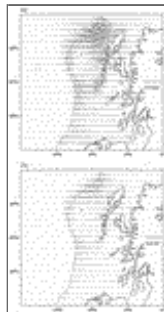
[Click on thumbnail for full-sized image.](#)

Fig. 3. Major and minor axis of the  $M_2$  tidal current ellipses at every third grid point computed using the  $q^2 - q^2 l$  model at (a) sea surface and (b) close to the seabed  $\sigma = -1.0$ , assuming a homogeneous sea region.



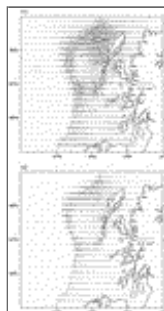
[Click on thumbnail for full-sized image.](#)

Fig. 4. Computed (a)  $O_1$  cotidal chart, (b)  $K_1$  cotidal chart, assuming a homogeneous sea region.

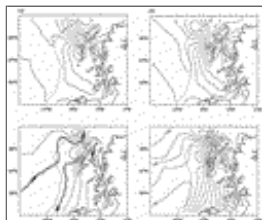


[Click on thumbnail for full-sized image.](#)

Fig. 5. Major and minor axis of the tidal current ellipses at every fourth grid point for (a) the  $O_1$  tide at the sea surface, (b) the  $O_1$  tide close to the seabed, (c) the  $K_1$  at the sea surface, and (d) the  $K_1$  tide close to the seabed, assuming a homogeneous sea region.

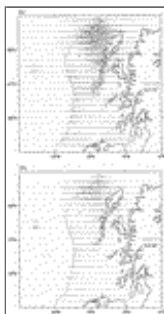


[Click on thumbnail for full-sized image.](#)



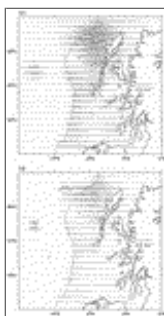
[Click on thumbnail for full-sized image.](#)

Fig. 6. Computed (a)  $O_1$  cotidal chart, (b)  $K_1$  cotidal chart, assuming a typical winter stratification.



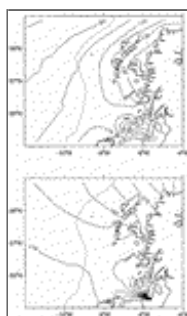
[Click on thumbnail for full-sized image.](#)

Fig. 7. As in [Fig. 5](#) but assuming a typical winter stratification.



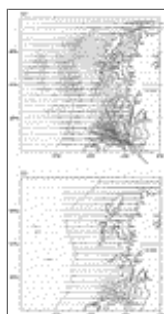
[Click on thumbnail for full-sized image.](#)

Fig. 7. (Continued)



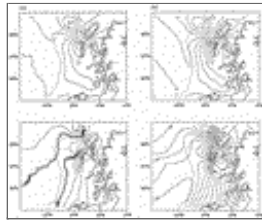
[Click on thumbnail for full-sized image.](#)

Fig. 8. Computed  $M_2$  cotidal chart, assuming a typical summer stratification.



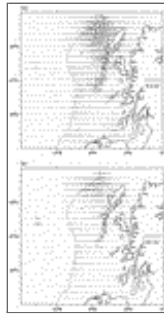
[Click on thumbnail for full-sized image.](#)

Fig. 9. Major and minor axis of the  $M_2$  tidal current ellipses at every fourth grid point at (a) sea surface and (b) close to the seabed, assuming typical summer stratification.



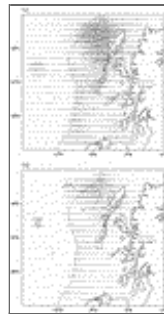
[Click on thumbnail for full-sized image.](#)

Fig. 10. Computed (a)  $O_1$  cotidal chart and (b)  $K_1$  cotidal chart, assuming a typical summer stratification.



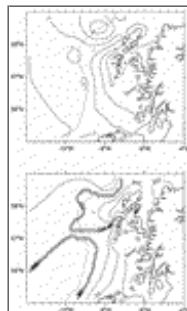
[Click on thumbnail for full-sized image.](#)

Fig. 11. As in [Fig. 5](#) but assuming a typical summer stratification.



[Click on thumbnail for full-sized image.](#)

Fig. 11. (Continued)



[Click on thumbnail for full-sized image.](#)

Fig. 12. Computed  $O_1$  cotidal chart, determined with the hybrid model, assuming a homogeneous sea region.





[Click on thumbnail for full-sized image.](#)

Fig. 13. Major and minor axis of the  $O_1$  tidal current ellipses at every fourth grid point at (a) sea surface and (b) seabed, determined with the hybrid model, assuming a homogeneous sea region.

*Corresponding author address:* Dr. Alan M. Davies, Proudman Oceanographic Laboratory, Bidston Observatory, Birkenhead, Merseyside L43 7RA, United Kingdom.

E-mail: [amd@pol.ac.uk](mailto:amd@pol.ac.uk)

[top ▲](#)



© 2008 American Meteorological Society [Privacy Policy and Disclaimer](#)  
Headquarters: 45 Beacon Street Boston, MA 02108-3693  
DC Office: 1120 G Street, NW, Suite 800 Washington DC, 20005-3826  
[amsinfo@ametsoc.org](mailto:amsinfo@ametsoc.org) Phone: 617-227-2425 Fax: 617-742-8718  
[Allen Press, Inc.](#) assists in the online publication of *AMS* journals.